



Cite this: *RSC Adv.*, 2021, **11**, 21384

Received 4th May 2021  
 Accepted 3rd June 2021

DOI: 10.1039/d1ra03469c  
[rsc.li/rsc-advances](http://rsc.li/rsc-advances)

## Gold nanoclusters as a GSH activated mitochondrial targeting photosensitizer for efficient treatment of malignant tumors<sup>†</sup>

Chen Fan, Shuyang Zhai, Wei Hu, Siyu Chi, Dan Song and Zhihong Liu \*

Gold nanoclusters (Au NCs), which have the characteristics of small size, near infrared (NIR) absorption and long triplet excited lifetime, have been used as a new type of photosensitizer for deep tissue photodynamic therapy (PDT). However, the therapeutic efficiency of the nano-system based on Au NCs still needs to be improved. Herein, we proposed a strategy using Mito-Au<sub>25</sub>@MnO<sub>2</sub> nanocomposites to achieve enhanced PDT. Au<sub>25</sub>(Capt)<sub>18</sub><sup>-</sup> nanoclusters were applied as photosensitizers and further modified with peptides to target mitochondrial and MnO<sub>2</sub> nanosheets to consume glutathione (GSH). In the presence of GSH, Mito-Au<sub>25</sub>@MnO<sub>2</sub> dis-integrated and Mito-Au<sub>25</sub> nanoparticles realized accurate mitochondrial targeting. Under the irradiation of 808 nm light, the nanocomposite ensured highly efficient PDT both *in vitro* and *in vivo* via oxidation pressure elevation and mitochondrial targeting in cancer cells.

## Introduction

Gold nanoclusters (Au NCs), consisting of a few to hundreds of gold atoms, exhibit discrete energy levels as their size ( $\sim 2$  nm) approaches the Fermi-wavelength of electrons.<sup>1,2</sup> Due to the unique molecule-like properties such as optical absorption and photoluminescence, Au NCs were widely used in biosensing,<sup>3</sup> imaging<sup>4,5</sup> and detection.<sup>6</sup> Furthermore, the photophysical property of Au NCs could be regulated by ligands to achieve strong near infrared (over 800 nm) absorption<sup>7</sup> and long lifetime of excited triplet state.<sup>8</sup> As we know, near infrared (NIR) excitation could reduce light scattering and absorption of endogenous molecules when interact with biological tissues, thus it's promising in tissue penetration and biological safety.<sup>9</sup> Consequently, Au NCs have been used as a new type of photosensitizers (PSs) for photodynamic therapy (PDT) which impart cytotoxicity *via* exciting photosensitizers in appropriate wavelengths of light.<sup>10</sup> More importantly, compared with PSs loaded on upconversion nanoparticles,<sup>11</sup> Au NCs improve the utilization efficiency of NIR excitation directly, without considering loading capacity and energy transfer efficiency.

In the meanwhile, the recent research suggests that MnO<sub>2</sub> nanosheets cooperating with PSs can elevate cellular uptake of PSs and upgrade oxidation pressure of cancer cells.<sup>12</sup> On the one hand, high concentration of glutathione (2–10 mM) alleviates

the PDT effect *via* consuming reactive oxygen species (ROS) generated by PSs.<sup>13,14</sup> MnO<sub>2</sub> nanosheets can be reduced to Mn<sup>2+</sup> by GSH, which will deplete GSH and strengthen oxidation pressure in cancer cells.<sup>12</sup> On the other hand, Au NCs with small size are prone to accumulate at the liver and spleen instead of tumor tissue.<sup>15</sup> MnO<sub>2</sub> nanosheets are suitable for enlarging the size of nanomaterials (up to 100–200 nm), which will improve the passive targeting ability of nanomaterials by enhanced permeability and retention effect (EPR). Unfortunately, there are still two main disadvantages of the assembled Au NCs and MnO<sub>2</sub> nanosheets. Firstly, complex charge conversion operation is needed before the negatively charged MnO<sub>2</sub> nanosheets are assembled with Au NCs. Secondly, this kind of nanocomposites still lack of mitochondrial targeting ability which is of significant importance to elevate the PDT efficiency.<sup>16</sup> Due to the short lifetime ( $<200$  ns) and limited movement distance ( $\sim 20$  nm), ROS are difficult to reach the core area of cancer cells and can't provide efficient tumor treatment capabilities.<sup>17</sup> Mitochondria play an important role in providing energy through oxidation of carbohydrates, fat and amino acids.<sup>18</sup> Besides, they are extremely fragile organelles in eukaryocyte cells because single-stranded mito-DNA is easier to be destroyed and thus accelerating the necrosis and apoptosis of cancer cells.<sup>19</sup> Therefore, nanocomposites which can target mitochondria will make full use of ROS and enhance PDT effect. Hence, constructing a new nano-system which can not only realize mitochondrial targeting but also facilitate direct electrostatic interaction with MnO<sub>2</sub> nanosheets is conducive to elevate PDT efficiency.

Herein, we utilized Au<sub>25</sub>(Capt)<sub>18</sub><sup>-</sup> nanoclusters, which have good chemical stability, anti-photobleaching ability and long excitation wavelength at NIR I region as PSs. Subsequently, mitochondrial targeting peptides (Fr-(Cha)-K-NH<sub>2</sub>) were

Key Laboratory of Analytical Chemistry for Biology and Medicine (Ministry of Education), College of Chemistry and Molecular Sciences, Wuhan University, Wuhan 430072, China. E-mail: zhliu@whu.edu.cn

<sup>†</sup> Electronic supplementary information (ESI) available: Synthesis and characterization of Mito-Au<sub>25</sub>@MnO<sub>2</sub> and supplementary spectral results. See DOI: 10.1039/d1ra03469c



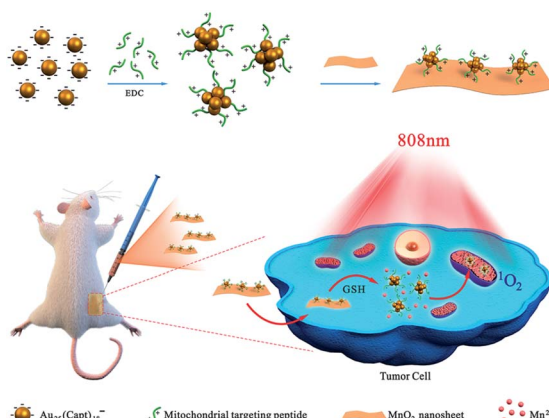


Fig. 1 Schematic diagram of assembling process and the mechanism of Mito-Au<sub>25</sub>@MnO<sub>2</sub> for *in vivo* PDT.

connected onto the surface of Au<sub>25</sub>(Capt)<sub>18</sub><sup>-</sup> nanoclusters to obtain Mito-Au<sub>25</sub> nanoparticles. Finally, the Mito-Au<sub>25</sub>@MnO<sub>2</sub> nanocomposites were obtained through electrostatic interaction between Mito-Au<sub>25</sub> nanoparticles and MnO<sub>2</sub> nanosheets. As illustrated in Fig. 1, the Mito-Au<sub>25</sub>@MnO<sub>2</sub> nanocomposite was an inactive photosensitizer before MnO<sub>2</sub> nanosheets were consumed by GSH. After cellular uptake, MnO<sub>2</sub> depleted GSH and the oxidation pressure increased in cancer cells. In the meanwhile, the nanocomposites disintegrated and Mito-Au<sub>25</sub> was released to achieve specific targeting of mitochondrial, thus elevating the utilization efficiency of ROS. Under the irradiation of 808 nm laser, we successfully realized high-efficient, deep seated and reliable PDT on HepG2 cells and 4T1 tumor bearing mice. Compared with traditional methods,<sup>20,21</sup> our study highlights the significance of subcellular targeting ability and GSH consumption efficiency.

## Results and discussion

### Characterization and photophysical properties of Au<sub>25</sub>(Capt)<sub>18</sub><sup>-</sup> nanoclusters

The Au<sub>25</sub>(Capt)<sub>18</sub><sup>-</sup> nanoclusters (abbreviated as Au<sub>25</sub>NCs) were prepared using a NaBH<sub>4</sub> reduction method at room temperature.<sup>22</sup> As shown in Fig. 2a, the obtained Au<sub>25</sub>NCs had good dispersity and uniformed size. The average hydrodynamic diameter of Au<sub>25</sub>NCs was  $2.515 \pm 0.546$  nm (Fig. 2a). Characteristic UV-Vis absorption spectra displayed at 670 nm, 450 nm and 400 nm (Fig. 2b) were in good accord with former research.<sup>23</sup> With the excitation at 561 nm, the maximum fluorescence emission wavelength was at 740 nm (Fig. S1†). X-ray photoelectron spectroscopy (XPS) was employed to demonstrate the elemental composition and valence state of Au<sub>25</sub>NCs. Binding energy of Au 4f<sub>5/2</sub> and Au 4f<sub>7/2</sub> were 87.6 eV and 84.1 eV, respectively (Fig. S2a†). The orbital binding energy of Au 4f<sub>7/2</sub> (84.1 eV) was between the binding energy of Au(0) (83.8 eV) and Au(i) (86.0 eV), which confirmed that Au(0) and Au(i) both existed in Au<sub>25</sub>NCs.<sup>24</sup> These results were consistent with former core-shell structure theory.<sup>25</sup> In addition, the binding energy of S 2p was 163.4 eV different from 168 eV (SO<sub>3</sub><sup>-</sup>), which confirmed

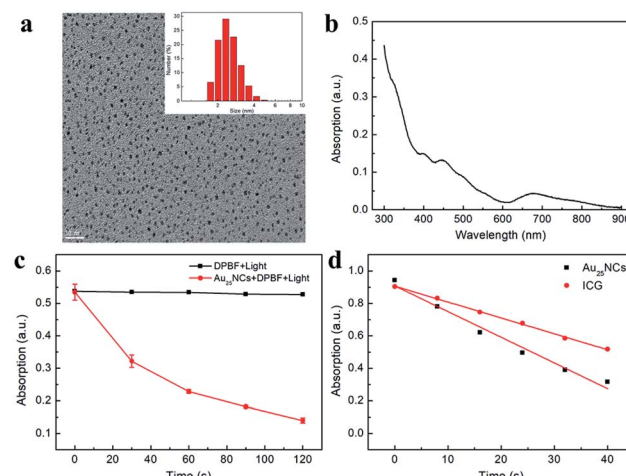


Fig. 2 (a) TEM image and size distribution of Au<sub>25</sub>NCs. (b) UV-Vis absorption spectra of Au<sub>25</sub>NCs. (c) Singlet oxygen generation of Au<sub>25</sub>NCs. Time dependent absorption changes at 412 nm of DMF solutions of DPBF (200  $\mu$ M) and Au<sub>25</sub>NCs (0 or 200  $\mu$ g mL<sup>-1</sup>) mixture upon irradiation at 808 nm light. (d) Singlet oxygen generation efficiency liner fitting of Au<sub>25</sub>NCs and indocyanine green (ICG).

the formation of Au-S bound (Fig. S2b†).<sup>26,27</sup> Therefore, we successfully synthesized Au<sub>25</sub>NCs.

Singlet oxygen ( $^1\text{O}_2$ ) generation ability of Au<sub>25</sub>NCs was monitored using singlet oxygen probe DPBF.<sup>28</sup> The UV-Vis spectrum of DPBF and Au<sub>25</sub>NCs mixture solution was recorded after each 30 s of irradiation with 808 nm light. As shown in Fig. 2c, with increasing irradiation time, the absorption value at 412 nm decreased gradually, indicating the formation of  $^1\text{O}_2$ . To our delight, the  $^1\text{O}_2$  quantum yield of Au<sub>25</sub>NCs was 9.12 times as much as indocyanine green (ICG), suggesting that Au<sub>25</sub>NCs could be used as excellent PSs to conduct PDT (Fig. 2d).

### Characterization of MnO<sub>2</sub> nanosheets

Two dimensional MnO<sub>2</sub> nanosheets were prepared by ultrasonicating of bulk MnO<sub>2</sub>.<sup>29</sup> The ultrathin MnO<sub>2</sub> nanosheets had a broad optical absorption spectrum (250–700 nm) and its maximum absorption wavelength was 371 nm (Fig. S3†). Transmission electron microscopy (TEM) and field emission scanning electron microscope (FESEM) images showed that MnO<sub>2</sub> nanosheets dispersed uniformly with sheet morphology (Fig. S4a, c and d†). The average hydrodynamic diameter of MnO<sub>2</sub> nanosheets was  $187.5 \pm 71.36$  nm (Fig. S4b†), and Fig. 3a indicated that these nanosheets were 1.2–1.6 nm in height, which were nearly two layers of MnO<sub>2</sub> nanosheet (the theoretical thickness of the single-layered MnO<sub>2</sub> nanosheet is 0.69–0.72 nm (ref. 30)). XPS graph showed that there were Mn 2p and O 1s in the spectrum (Fig. S5a†). It could be found that the binding energy of Mn 2p<sub>3/2</sub> and Mn 2p<sub>1/2</sub> were 641.3 eV and 653.2 eV, respectively (Fig. S5b†), with a spin-energy separation of 11.9 eV, which confirmed the formation of Mn(IV)O<sub>2</sub> nanosheets.<sup>31</sup> The reaction between MnO<sub>2</sub> and GSH was tested. With the increasing concentration of GSH, the absorption of MnO<sub>2</sub> at 371 nm decreased gradually (Fig. S6†), which indicated the reaction of MnO<sub>2</sub> and GSH was concentration dependent.



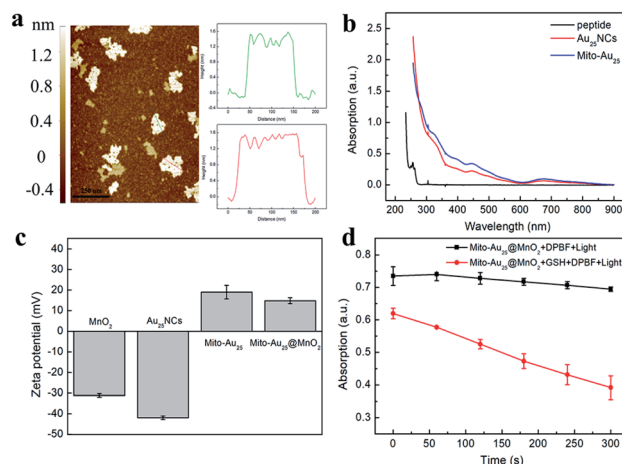


**Fig. 3** (a) Atomic force microscopy (AFM) image and corresponding height profile of  $\text{MnO}_2$  nanosheets. Scale bar: 250 nm. (b) UV-Vis absorption spectra of mitochondrial targeting peptide,  $\text{Au}_{25}\text{NCs}$  and  $\text{Mito-Au}_{25}$ . (c) Zeta potential of  $\text{MnO}_2$ ,  $\text{Au}_{25}\text{NCs}$ ,  $\text{Mito-Au}_{25}$  and  $\text{Mito-Au}_{25}@\text{MnO}_2$ . (d) GSH (0 or 200  $\mu\text{M}$ ) dominated activable  ${}^1\text{O}_2$  generation of  $\text{Mito-Au}_{25}@\text{MnO}_2$ . Time dependent absorption changes at 412 nm of DPBF (200  $\mu\text{M}$ ) and  $\text{Mito-Au}_{25}@\text{MnO}_2$  (200  $\mu\text{g mL}^{-1}$ ) mixture solution upon irradiation at 808 nm.

### Characterization and photophysical properties of $\text{Mito-Au}_{25}$ nanoparticles and $\text{Mito-Au}_{25}@\text{MnO}_2$ nanocomposites

The  $\text{Mito-Au}_{25}$  nanoparticles were synthesized through biological coupling reaction between mitochondrial targeting peptide and  $\text{MnO}_2$  nanosheets. Compared with  $\text{Au}_{25}\text{NCs}$ , the size of these nanoparticles increased obviously (Fig. S7†), which was probably due to charge inversion and electrostatic interaction between  $\text{Mito-Au}_{25}$  and  $\text{Au}_{25}\text{NCs}$ . Furthermore, a new UV-Vis absorption peak emerged at 276 nm after mitochondrial targeting peptide was modified onto the surface of  $\text{Au}_{25}\text{NCs}$ , which was a little red shift referring to the characteristic absorption at 260 nm of mitochondrial targeting peptide (Fig. 3b). Fourier-transform infrared spectroscopy (FTIR) further proved the change of functional group at  $3424\text{ cm}^{-1}$  (Fig. S8†). We monitored the  ${}^1\text{O}_2$  generation ability of  $\text{Mito-Au}_{25}$  to test whether the modification of peptide would influence the photophysical property of  $\text{Au}_{25}\text{NCs}$ . As shown in Fig. S9a,† the absorption at 412 nm of DPBF and  $\text{Mito-Au}_{25}$  mixture solution decreased via a time dependent mode indicating the formation of  ${}^1\text{O}_2$ . Three parallel experiments were conducted and confirmed the efficient  ${}^1\text{O}_2$  generation of  $\text{Mito-Au}_{25}$  nanoparticles (Fig. S9b†).

Zeta potential of  $\text{Au}_{25}\text{NCs}$ ,  $\text{Mito-Au}_{25}$  and  $\text{MnO}_2$  nanosheets were measured before assembling (Fig. 3c).  $\text{Au}_{25}\text{NCs}$  were negatively charged ( $-41.9\text{ mV}$ ). After modification of mitochondrial targeting peptide,  $\text{Mito-Au}_{25}$  showed the average zeta potential of  $17.2\text{ mV}$ . The average zeta potential of  $\text{MnO}_2$  nanosheets was  $-30.4\text{ mV}$ , which presented an ideal charge state for electrostatic assembling. Finally,  $\text{Mito-Au}_{25}@\text{MnO}_2$  nanocomposites were obtained through electrostatic interaction between positively charged  $\text{Mito-Au}_{25}$  nanoparticles and negatively charged  $\text{MnO}_2$  nanosheets. The average zeta potential of nanocomposites was  $14.1\text{ mV}$ . UV-Vis absorption

spectrum in Fig. S10† showed no characteristic absorption peak of  $\text{Au}_{25}$  NCs in supernatant after centrifugation procedure, which meant that 2.5 mg  $\text{Mito-Au}_{25}$  was completely assembled with 0.08 mg  $\text{MnO}_2$  nanosheets.

TEM was utilized to observe the morphology of  $\text{Mito-Au}_{25}@\text{MnO}_2$  nanocomposites. As shown in Fig. S11a,† the nanocomposites presented good dispersity and no evident aggregation occurred. But the  $\text{Mito-Au}_{25}$  nanoparticles on the surface of  $\text{MnO}_2$  nanosheets were not clear. From the high-magnification image (Fig. S11b†), the  $\text{Mito-Au}_{25}$  nanoparticles were distinctively observed on the surface of nanocomposites and the nanomaterials presented clear sheet morphology. Furthermore, freely dispersed  $\text{Mito-Au}_{25}$  nanoparticles didn't exist. These results further confirmed the formation of  $\text{Mito-Au}_{25}@\text{MnO}_2$ . The ultimately obtained  $\text{Mito-Au}_{25}@\text{MnO}_2$  displayed sheets morphology. Compared with mesoporous<sup>32</sup> and nanoparticle<sup>33</sup> structures, ultrathin nanosheets have more sensitive responsibility to tumor microenvironment (TME),<sup>34</sup> which can not only lead to fast GSH consumption and oxidation pressure elevation in cancer cells, but also efficiently release photosensitizer to generate  ${}^1\text{O}_2$ . Therefore, nanosheets morphology of  $\text{Mito-Au}_{25}@\text{MnO}_2$  nanocomposites is benefit to the improvement of PDT efficiency. In the meanwhile,  $\text{Mito-Au}_{25}@\text{MnO}_2$  nanocomposites maintained good thermal stability (Fig. S12†), which was also conducive to better PDT efficiency.

As expected,  $\text{Mito-Au}_{25}@\text{MnO}_2$  nanocomposites could hardly generate  ${}^1\text{O}_2$  under 808 nm light irradiation (Fig. 3d). However, after GSH consuming part of  $\text{MnO}_2$  nanosheets (Fig. S13†), the  $\text{Mito-Au}_{25}$  nanoparticles released from nanocomposites still could generate  ${}^1\text{O}_2$  (Fig. 3d). The results verified the GSH activated PDT property of  $\text{Mito-Au}_{25}@\text{MnO}_2$  nanocomposites evidently.

### *In vitro* mitochondrial targeting ability and PDT efficiency

In order to get ready for subsequent cellular experiments, we first tested the cellular uptake efficiency. To HepG2 cells, the optimum cellular uptake time of  $\text{Au}_{25}\text{NCs}$  and  $\text{Mito-Au}_{25}@\text{MnO}_2$  were 2 h and 4 h, respectively (Fig. S14–S16†). The difference of cellular uptake time was probably related to the charge state, particle size and morphology of nanomaterials.<sup>35–37</sup> Targeting ability of  $\text{Mito-Au}_{25}$  might also prolong cell retention time of nanocomposites. Mito Tracker Green (MTG) was used to compare mitochondrial colocalization efficiency of  $\text{Au}_{25}\text{NCs}$  and  $\text{Mito-Au}_{25}$ . A small part overlap of fluorescence signal of  $\text{Au}_{25}\text{NCs}$  and MTG was observed (Fig. S17†), indicating that  $\text{Au}_{25}\text{NCs}$  didn't have mitochondria specificity. On the contrary, thanks to the mitochondrial targeting peptide, the red fluorescence from  $\text{Mito-Au}_{25}$  (Fig. 4a) and the green fluorescence from MTG (Fig. 4b) showed significant overlap (Fig. 4c and e). The colocalization degree also intuitively showed in Fig. 4d with a Pearson's correlation factor of 0.965. All these statistics proved that  $\text{Mito-Au}_{25}$  could efficiently localized in mitochondria after cellular uptake.

DCFH-DA as a kind of ROS probe was used to detect  ${}^1\text{O}_2$  generated in HepG2 cells.<sup>38</sup> After oxidization by  ${}^1\text{O}_2$  to DCF, it



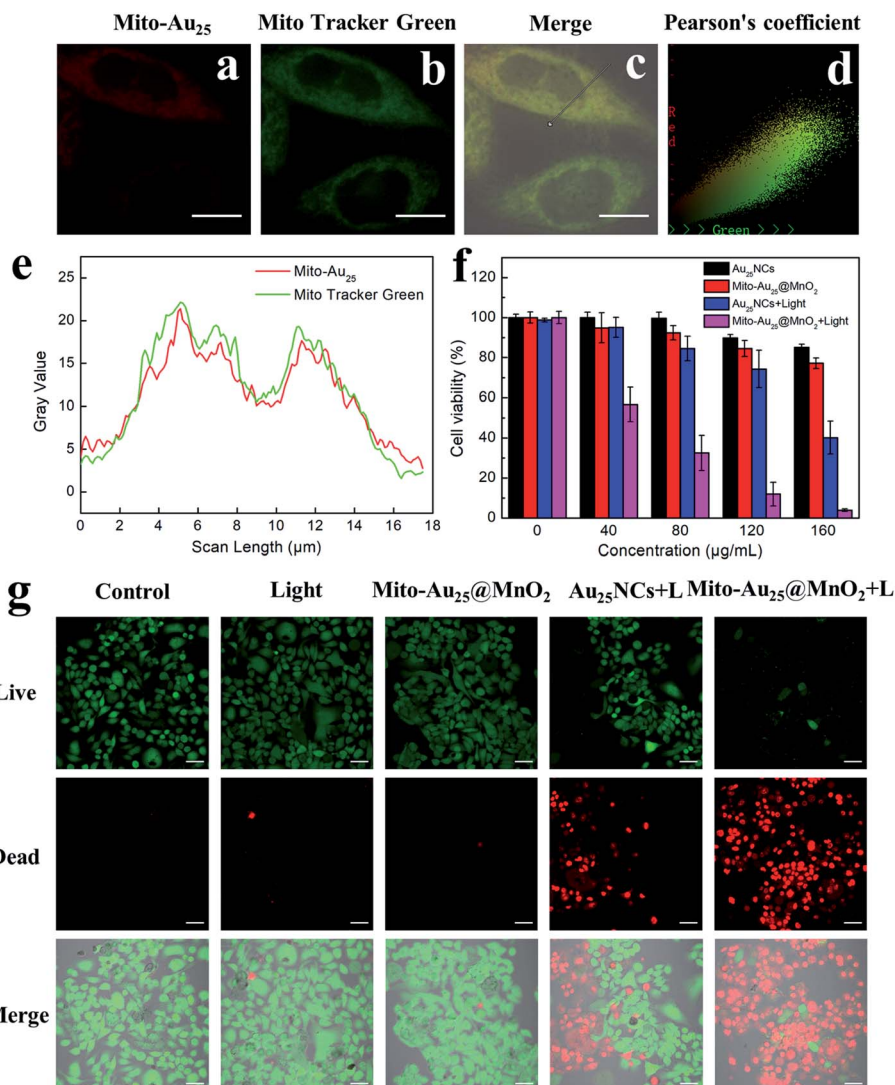


Fig. 4 Fluorescence signal of (a) Mito-Au<sub>25</sub> (160  $\mu\text{g mL}^{-1}$ ,  $\lambda_{\text{ex}} = 488 \text{ nm}$ ,  $\lambda_{\text{em}} = 650\text{--}760 \text{ nm}$ ) and (b) Mito Tracker Green (0.2  $\mu\text{M}$ ,  $\lambda_{\text{ex}} = 488 \text{ nm}$ ,  $\lambda_{\text{em}} = 500\text{--}550 \text{ nm}$ ) in HepG2 cells. (c) Overlay of (a) and (b) in bright field. Scale bar: 10  $\mu\text{m}$ . Pearson's colocalization coefficient (d) and profile gray value (e) of Mito-Au<sub>25</sub> and Mito Tracker Green. (f) Cell viability of HepG2 cells treated with Au<sub>25</sub>NCs or Mito-Au<sub>25</sub>@MnO<sub>2</sub> and irradiated at 808 nm (0 or 2.4  $\text{W cm}^{-2}$ ) through CCK-8 assay. (g) Confocal images of Calcein-AM and PI stained HepG2 cells with different treatments (PBS, 808 nm light, Mito-Au<sub>25</sub>@MnO<sub>2</sub>, Au<sub>25</sub>NCs + 808 nm light and Mito-Au<sub>25</sub>@MnO<sub>2</sub> + 808 nm light). Scale bar: 50  $\mu\text{m}$ .

showed bright green fluorescence under 488 nm excitation. As shown in Fig. S18,† HepG2 cells treated with Mito-Au<sub>25</sub>@MnO<sub>2</sub> or 808 nm light nearly didn't exhibit green fluorescence signal. This phenomenon was similar with control group. While the cells treated with Mito-Au<sub>25</sub>@MnO<sub>2</sub> followed by 808 nm light irradiation showed significant green fluorescence emission, indicating the generation of  ${}^1\text{O}_2$  in HepG2 cells.

To estimate the PDT efficiency of the prepared nanocomposites, four groups of HepG2 cells were treated under different conditions for 24 h and the cell viability were measured by CCK-8 assay. As shown in Fig. 4f, Au<sub>25</sub>NCs, Mito-Au<sub>25</sub>@MnO<sub>2</sub> and 808 nm light had favourable biocompatibility because cells treated in these groups remained a high viability over 80%. However, when first incubated with Au<sub>25</sub>NCs or Mito-Au<sub>25</sub>@MnO<sub>2</sub> and then accepted 808 nm light treatment, the cell

viability sharply reduced to 40% and 4%, respectively (Fig. 4f). The result demonstrated superior cytotoxicity of Mito-Au<sub>25</sub>@MnO<sub>2</sub> under 808 nm light irradiation. Furthermore, Calcein-AM and PI staining assay intuitively revealed the killing effect of different treatments (Fig. 4g). Taken together, the above results had confirmed that Mito-Au<sub>25</sub>@MnO<sub>2</sub> had higher PDT efficiency than Au<sub>25</sub>NCs *in vitro*.

#### *In vivo* PDT efficiency

Before investigating the *in vivo* PDT effect, the biocompatibility of Mito-Au<sub>25</sub>@MnO<sub>2</sub> (0, 5, and 10  $\text{mg kg}^{-1}$ ) was evaluated. The results illustrated that the increasing trend of body weight from different group of mice had no difference during 14 days after injection (Fig. S19†), and the biochemical indicators of three groups of mice were all in normal range (Fig. S20†). H&E



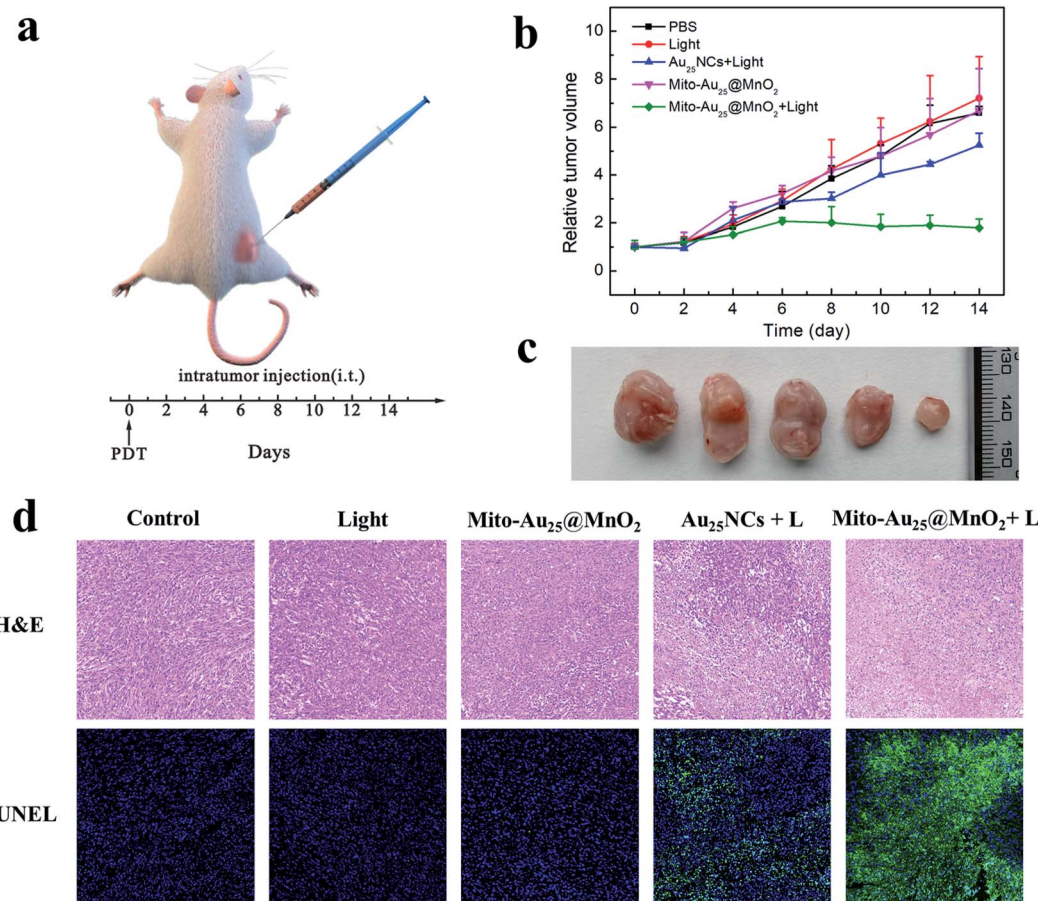


Fig. 5 (a) Schematic illustration of *in vivo* antitumor study. (b) Relative tumor volume of mice with various treatments. (c) Representative photographs of the corresponding excised tumor (from left to right were given PBS, 808 nm light, Mito-Au<sub>25</sub>@MnO<sub>2</sub>, Au<sub>25</sub>NCs + 808 nm light and Mito-Au<sub>25</sub>@MnO<sub>2</sub> + 808 nm light, respectively). (d) Images of H&E and TUNEL stained tumor tissues. Scale bar: 100  $\mu$ m.

staining figures indicated few obvious injuries in major organs (Fig. S21†). These results suggested that Mito-Au<sub>25</sub>@MnO<sub>2</sub> had favourable biocompatibility.

The 4T1 tumor bearing mice model was constructed to compare the therapeutic efficiency of Au<sub>25</sub>NCs and Mito-Au<sub>25</sub>@MnO<sub>2</sub>. When the tumor volume reached 100–150  $\text{mm}^3$ , the mice were divided into five groups randomly and were given different treatments: (1) PBS; (2) 808 nm light irradiation (1.46  $\text{W cm}^{-2}$ ); (3) Mito-Au<sub>25</sub>@MnO<sub>2</sub>; (4) Au<sub>25</sub>NCs + 808 nm light irradiation and (5) Mito-Au<sub>25</sub>@MnO<sub>2</sub> + 808 nm light irradiation. All these materials (PBS, Au<sub>25</sub>NCs and Mito-Au<sub>25</sub>@MnO<sub>2</sub>) were directly injected into the tumor (Fig. 5a). The body weight of mice in five groups reflected the same increasing trend (Fig. S22†), and the H&E staining results indicated few damages in major organs (Fig. S23†), verifying that all the experimental treatments had hardly adverse effect to the mice. As shown in Fig. 5b and c, 808 nm light or Mito-Au<sub>25</sub>@MnO<sub>2</sub> didn't affect the growth rate of tumor tissues and these two groups showed the same growing trend with blank control. On the contrary, the tumor growth rate of mice treated with nanomaterials together with 808 nm laser slowed down, and Mito-Au<sub>25</sub>@MnO<sub>2</sub> was more effective than Au<sub>25</sub>NCs in inhibiting tumor growth. Besides, the tumor tissues in different group were excised for

H&E and TUNEL staining. As expected, the group treated with Mito-Au<sub>25</sub>@MnO<sub>2</sub> and 808 nm light showed the highest level of tumor tissue damage (Fig. 5d), indicating that GSH consumption ability and mitochondrial targeting ability of nanocomposites could remarkably enhance the therapeutic efficiency.

## Conclusions

In summary, we constructed an efficient nanocomposite system named Mito-Au<sub>25</sub>@MnO<sub>2</sub> and fulfilled enhanced PDT. The nano-system consisting of Au<sub>25</sub>(Capt)<sub>18</sub><sup>−</sup>, mitochondrial targeting peptide and GSH consumable MnO<sub>2</sub> nanosheets was structured through chemical modification and electrostatic interaction. Mito-Au<sub>25</sub>@MnO<sub>2</sub> nanocomposite was an inactive photosensitizer before GSH decomposed MnO<sub>2</sub> nanosheets. Once MnO<sub>2</sub> nanosheets were depleted, the nanocomposite turned into Mito-Au<sub>25</sub> nanoparticles. With the consumption of GSH, oxidation pressure elevated and Mito-Au<sub>25</sub> anchored mitochondria in cancer cells. Cell viability decreased remarkably to 4% under 808 nm light irradiation by fully utilization of ROS. Eventually, we realized efficient therapy of 4T1 tumor bearing mice. These results confirmed that GSH consumption



and mitochondrial targeting were promising strategies for PDT. We conceive that this study will encourage further exploitation on PDT based on Au NCs.

## Ethical statement

All animal studies were performed according to the Guidelines for the Care and Use of Laboratory Animals of the Chinese Animal Welfare Committee and approved by the Institutional Animal Care and Use Committee, Wuhan University Center for Animal Experiment, Wuhan, China.

## Conflicts of interest

The authors declare no competing financial interest.

## Acknowledgements

This work was supported by National Natural Science Foundation of China (No. 21625503).

## References

- Y. Tao, M. Q. Li, J. S. Ren and X. G. Qu, *Chem. Soc. Rev.*, 2015, **44**, 8636–8663.
- R. C. Jin, *Nanoscale*, 2010, **2**, 343–362.
- Y. C. Wang, Y. Wang, F. B. Zhou, P. Kim and Y. N. Xia, *Small*, 2012, **8**, 3769–3773.
- C. J. Sun, H. Yang, Y. Yuan, X. Tian, L. M. Wang, Y. Guo, L. Xu, J. L. Lei, N. Gao, G. J. Anderson, X. J. Liang, C. Y. Chen, Y. L. Zhao and G. J. Nie, *J. Am. Chem. Soc.*, 2011, **133**, 8617–8624.
- X. R. Song, W. Zhu, X. G. Ge, R. F. Li, S. H. Li, X. Chen, J. B. Song, J. P. Xie, X. Y. Chen and H. H. Yang, *Angew. Chem., Int. Ed.*, 2020, **59**, 2–9.
- H. P. Peng, M. L. Jian, Z. N. Huang, W. J. Wang, H. H. Deng, W. H. Wu, A. L. Liu, X. H. Xia and W. Chen, *Biosens. Bioelectron.*, 2018, **105**, 71–76.
- Z. K. Wu and R. C. Jin, *Nano Lett.*, 2010, **10**, 2568–2573.
- H. Kawasaki, S. Kumar, G. Li, C.-J. Zeng, D. R. Kauffman, J. Yoshimoto, Y. Iwasaki and R.-C. Jin, *Chem. Mater.*, 2014, **26**, 2777–2788.
- Y. F. Tang, F. Pei, X. M. Lu, Q. L. Fan and W. Huang, *Adv. Opt. Mater.*, 2019, **7**, 1900917.
- R. Ho-Wu, S.-H. Yau and T. Goodson, *J. Phys. Chem. B*, 2017, **121**, 10073–10080.
- D. Song, S.-Y. Chi, X. Li, C.-X. Wang, Z. Li and Z.-H. Liu, *ACS Appl. Mater. Interfaces*, 2019, **11**, 41100–41108.
- H. H. Fan, G. B. Yan, Z. L. Zhao, X. X. Hu, W. H. Zhang, H. Liu, X. Y. Fu, T. Fu, X. B. Zhang and W. H. Tan, *Angew. Chem., Int. Ed.*, 2016, **55**, 5477–5482.
- Y. F. Tu, F. Peng, P. B. White and D. A. Wilson, *Angew. Chem., Int. Ed.*, 2017, **56**, 7620–7624.
- F. Jiang, A. M. Robin, M. Katakowski, L. Tong, M. Espiritu, G. Singh and M. Chopp, *Lasers Med. Sci.*, 2003, **18**, 128–133.
- Q. F. Zhuang, H. Y. Jia, L. B. Du, Y. C. Li, Z. Chen, S. P. Huang and Y. Liu, *Biosens. Bioelectron.*, 2014, **55**, 76–82.
- H. T. Bi, Y. L. Dai, P. P. Yang, J. T. Xu, D. Yang, S. L. Gai, F. He, G. H. An, C. N. Zhong and J. Lin, *Chem. Eng. J.*, 2019, **356**, 543–553.
- L. M. Pan, J. N. Liu and J. L. Shi, *Adv. Funct. Mater.*, 2014, **24**, 7318–7327.
- S. Fulda, L. Galluzzi and G. Kroemer, *Nat. Rev. Drug Discovery*, 2010, **9**, 447–464.
- B. Yan, L. F. Dong and J. Neuzil, *Mitochondrion*, 2016, **26**, 86–93.
- Q. Chen, J. Chen, Z. Yang, L. Zhang, Z. Dong and Z. Liu, *Nano Res.*, 2018, **11**, 5657–5669.
- D. Yang, G. Yang, S. Gai, F. He, G. An, Y. Dai, R. Lv and P. Yang, *Nanoscale*, 2015, **7**, 19568–19578.
- S. Kumar and R. C. Jin, *Nanoscale*, 2012, **4**, 4222–4227.
- M. Z. Zhu, C. M. Aikens, F. J. Hollander, G. C. Schatz and R. C. Jin, *J. Am. Chem. Soc.*, 2008, **130**, 5883–5885.
- Y. Negishi, K. Nobusada and T. Tsukuda, *J. Am. Chem. Soc.*, 2005, **127**, 5261–5270.
- M. Z. Zhu, C. M. Aikens, F. J. Hollander, G. C. Schatz and R. C. Jin, *J. Am. Chem. Soc.*, 2008, **130**, 5883–5885.
- Z. H. Tang, B. Xu, B. H. Wu, M. W. Germann and G. L. Wang, *J. Am. Chem. Soc.*, 2010, **132**, 3367–3374.
- L. Shang, N. Azadfar, F. Stockmar, W. Send, V. Trouillet, M. Bruns, D. Gerthsen and G. U. Nienhaus, *Small*, 2011, **7**, 2614–2620.
- S. O. McDonnell, M. J. Hall, L. T. Allen, A. Byrne, W. M. Gallagher and D. F. O'Shea, *J. Am. Chem. Soc.*, 2005, **127**, 16360–16361.
- Z. L. Zhao, H. H. Fan, G. F. Zhou, H. R. Bai, H. Liang, R. W. Wang, X. B. Zhang and W. H. Tan, *J. Am. Chem. Soc.*, 2014, **136**, 11220–11223.
- Z. P. Ma, G. J. Shao, Y. Q. Fan, G. L. Wang, J. J. Song and D. J. Shen, *ACS Appl. Mater. Interfaces*, 2016, **8**, 9050–9058.
- W. P. Fan, W. B. Bu, B. Shen, Q. J. He, Z. W. Cui, Y. Y. Liu, X. P. Zheng, K. L. Zhao and J. L. Shi, *Adv. Mater.*, 2015, **27**, 4155–4161.
- G. Yang, L. Xu, Y. Chao, J. Xu, X. Sun, Y. Wu, R. Peng and Z. Liu, *Nat. Commun.*, 2017, **8**, 902.
- X. Liu, K. Tian, J. Zhang, M. Zhao, S. Liu, Q. Zhao and W. Huang, *ACS Appl. Bio Mater.*, 2019, **2**, 1225–1232.
- Z. Liu, S. Zhang, H. Lin, M. Zhao, H. Yao, L. Zhang, W. Peng and Y. Chen, *Biomaterials*, 2018, **155**, 54–63.
- V. Hirsch, C. Kinnear, M. Moniatte, B. Rothen-Rutishauser, M. J. D. Clift and A. Fink, *Nanoscale*, 2013, **5**, 3723–3732.
- B. D. Chithrani, A. A. Ghazani and W. C. W. Chan, *Nano Lett.*, 2006, **6**, 662–668.
- B. D. Chithrani and W. C. W. Chan, *Nano Lett.*, 2007, **7**, 1542–1550.
- S. Shen, C. L. Zhu, D. Huo, M. X. Yang, J. J. Xue and Y. N. Xia, *Angew. Chem., Int. Ed.*, 2017, **56**, 8801–8804.

